A Novel Cell Force Sensor for Quantification of Traction during Cell Spreading and Contact Guidance

N. Tymchenko,* J. Wallentin,* S. Petronis,* L. M. Bjursten,† B. Kasemo,* and J. Gold*
*Applied Physics, Chalmers University of Technology, Göteborg, Sweden; and †Department of Clinical Sciences, Faculty of Medicine, Lund University, Lund, Sweden

ABSTRACT In this work, we present a ridged, microfabricated, force sensor that can be used to investigate mechanical interactions between cells exhibiting contact guidance and the underlying cell culture substrate, and a proof-of-function evaluation of the force sensor performance. The substrates contain arrays of vertical pillars between solid ridges that were microfabricated in silicon wafers using photolithography and deep reactive ion etching. The spring constant of the pillars was measured by atomic force microscopy. For time-lapse experiments, cells were seeded on the pillared substrates and cultured in an on-stage incubator on a microscope equipped with reflected differential interference contrast optics. Endothelial cells (ECs) and fibroblasts were observed during attachment, spreading, and migration. Custom image analysis software was developed to resolve cell borders, cell alignment to the pillars and migration, displacements of individual pillars, and to quantify cell traction forces. Contact guidance classification was based on cell alignment and movement angles with respect to microfabricated ridges, as well as cell elongation. In initial investigations made with the ridged cell force sensor, we have observed contact guidance in ECs but not in fibroblast cells. A difference in maximal amplitude of mechanical forces was observed between a contact-guided and non-contact-guided, but mobile, EC. However, further experiments are required to determine the statistical significance of this observation. By chance, we observed another feature of cell behavior, namely a reversion of cell force direction. The direction of forces measured under rounded fibroblast cells changed from outwards during early cell attachment to inwards during further observation of the spreading phase. The range of forces measured under fibroblasts (up to 138 nN) was greater than that measured in EC (up to 57 nN), showing that the rigid silicon sensor is capable of resolving a large range of forces, and hence detection of differences in traction forces between cell types. These observations indicate proof-of-function of the ridged cell force sensor to induce contact guidance, and that the pillared cell force sensor constructed in rigid silicon has the necessary sensitivity to detect differences in traction force vectors between different cell phenotypes and morphologies.

INTRODUCTION

Most mammalian cells are anchorage dependent; that is, they require a surface for attachment, growth, and proliferation. As a result, a mechanical interaction exists between the cell and the underlying substrate. Mechanical signals play a significant role in the signaling system regulating cell and tissue development and physiology (1,2). The normal extracellular matrix (ECM) to which cells attach is a viscoelastic composite that comprises stiff elastic fibers of cell-secreted proteins embedded in a polysaccharide gel. In addition to the chemical cues provided by these proteins, the cell senses, and is able to actively remodel, the mechanical environment. The influence of different modulus substrates on cell responses, and the investigation of mechanical interactions between cells and their growth substrates, is therefore of great interest.

The study of cell-material interactions is a broad field of research, including cell adhesion, migration, proliferation, and differentiation, as well as the traction forces generated by adherent cells. In the past decades, a variety of substrates have been used for the study of cell traction forces. Traction forces in chick heart fibroblasts cultured on silicone rubber membranes were quantified based on the morphology of deformations observed in the films (3), and this method was later refined for use with keratocytes (4). The usage of deformable cell culture substrates further progressed with the use of synthetic hydrogels like polyacrylamide coated with collagen (5), as well as with embedded fluorescent particles for for measurement of substrate deformations by the cell (6,7). Other hydrogels that have been used include agarose (8), fibrin (9), and collagen (10). Variation of total gel composition, component concentration, or extent of cross-linking could be used to produce substrates of varying stiffnesses (5,6,11), often with some surface modification to facilitate cell adhesion. The modulus of such gel substrates needs to be low enough to enable detectable substrate deformation within the range of forces produced by attaching, spreading, and migrating cells.

A major drawback of using flexible substrates for cell force detection is that the force indicators, whether wrinkles or embedded particles, are mechanically coupled. Advanced computer modeling is required to convert the deformations into forces, and these force measurements may only be reliable at cell level. Mapping of focal adhesions can increase the accuracy (12), but ultimately the measurements are still

Submitted August 1, 2006, and accepted for publication February 27, 2007.

Address reprint requests to Sarunas Petronis, Asst. Prof. Applied Physics, Chalmers University of Technology, 412 96 Göteborg, Sweden. Tel.: 46-31-772-3368; E-mail: petronis@fy.chalmers.se.

Editor: Kevin D. Costa.

0006-3495/07/07/335/11 $2.00

doi: 10.1529/biophysj.106.093302

coupled, both within a single cell, and between neighboring cells. Hence, quantification of cell-substrate interactions on these types of continuous substrates is complicated. As an alternative, systems of discrete cantilevers, henceforth termed ''pillars'', were developed to obtain truly independent measurements and simplify the force calculations.

In the last decade, pillared substrates have become a popular alternative to the continuous substrates. A sensor was developed using micromachined silicon wafers, incorporating horizontally oriented pillars with independent force-sensing attachment pads (13). The force measurements (up to 100 nN under chick embryo fibroblasts) were still limited because forces could not be measured along the axis of the embedded cantilever. Moreover, it was impossible to decouple force direction and magnitude. Other studies have utilized vertical pillars, which do not have such limitations as they can freely bend into all directions and are not coupled to each other. Most commonly used are poly-dimethyl-siloxane (PDMS) elastomer pillars, as they are easy to produce by replication from a micromachined mold. PDMS is an elastic, biocompatible material that is optically transparent. PDMS microneedles, functionalized with fibronectin to facilitate cell attachment, could be used to measure forces in the range of 5–90 nN in smooth muscle cells (14). Primary neonatal rat cardiomyocytes were cultured on the flat surface surrounding PDMS pillars, grown to confluence, and then observed deflecting the pillars with forces of up to 3.5 μN (15). Given the elasticity of this material, vertical pillars do not need to have a high aspect ratio to obtain the desired spring constant, and may have heights on the order of a cell, or less. It is therefore a risk that cells reach down to the base of the pillars. Cell force measurements performed with vertical pillars might also influence cell biological reactions by the specific topography provided by the pillar arrays. As cells should attach mainly to the tops of the pillars, they are presented with a limited attachment area that might significantly affect morphology and functions of anchorage dependant cells (16). Thus geometry of the pillars and their distribution has to be taken into account when designing vertical pillar-based force sensors.

Previously, we have also shown that vertical pillars micromachined in a stiff biocompatible material, such as silicon, can be used to measure cell forces (17). These sensors have improved optical contrast compared with PDMS, due to their flatness and high substrate reflectivity, theoretically allowing higher precision force measurements to be achieved. When micromachining in silicon, it is possible to manipulate both the organization and aspect-ratio of pillars, allowing subcellular force measurement, and pillars of varying spatial arrangements and elastic properties. This type of manufacturing also ensures the production of well-controlled topographical substrates with the possibility for enlarged cell attachment area on the top of pillars. An interesting possibility exists of incorporating additional features to influence the migration of cells. Since the patterning of substrate ridges is known to affect cell shape and motion (18), we predict these substrates may be designed to influence cell movement, a property desirable for modern biomaterials. Contact guidance (19) is a phenomenon whereby a cell that senses a step, in this case the trenches containing pillars adjacent to ridges, will tend to follow the direction of the step, becoming elongated. The magnitude of topographical alignment is mainly dependent on the depth of the trenches (20). Even with the presence of an opposing (discontinuous) chemical pattern, MC3T3-E1 cells were seen to be influenced by the underlying topographical pattern of 4 μm (21). Though in the case of BHK cells, whereas both topography and chemistry could induce alignment, a continuous chemical pattern was more dominant (22). Hence cellular reaction to chemical and topographical substrate cues is dependent on cell type.

In this article we explore further the application of micromachined silicon substrates patterned with arrays of pillars in between solid ridges. Such substrates are intended to observe cellular traction force distribution and dynamics during cell spreading, migration, and topographical contact guidance. Human vascular endothelial cells (EC) and fibroblasts were able to attach, spread, and migrate on the top of microfabricated silicon substrates and, as a result, deflect the pillars underneath the cells. As multiple pillars were positioned under each cell, the observed deflections were used for the detection of forces distributed with subcellular lateral resolution in the nanonewton magnitude range.

MATERIALS AND METHODS

Microfabrication and calibration of force-sensing substrates

Silicon substrates containing ridges alternating with arrays of embedded vertical pillars were microfabricated and calibrated as previously described (17). In brief, the microfabrication was performed in two major steps:

1. fabrication of the attachment pads in silicon dioxide layer by photolithography and wet or dry oxide etching (patterned photoresist layer serves as the etching resistant mask defining shape and distribution of the pads);
2. fabrication of the pillars by etching deep trenches around the attachment pads (silicon dioxide pads serve as the etching resistant mask determining diameter and distribution of the cantilevers). In the first step, a 430-nm thick thermal oxide (SiO_2) film on 3-inch Si-(001) wafers was photolithographically patterned using S-1813 Shipley Microposit photoresist (Shipley Europe Ltd., Coventry, UK) followed by dry plasma etching (CH_4/C_3F_8) or wet buffered oxide etching (HF/NH_4F). Afterwards, the patterned oxide layer served as a mask for deep silicon etching performed in an inductively coupled plasma system (STS Multiplex from Surface Technology Systems, Newport, UK) by multiple cycling of etching and sidewall passivation steps to maintain anisotropy (Robert Bosch GmbH process). After the etching was complete, generating 51 μm height cantilevers, the residues of the photoresist were stripped off in oxygen plasma (PlasmaTherm Batchtop VIII PE/RIE, Plasma-Therm Inc., St. Petersburg, FL). The wafer then was cut in 5×5 mm^2 chips, each containing a force-sensing area of 3×3 mm^2.

Atomic force microscopy (AFM; Dimension 3000 NanoScope, Veeco Instruments, Woodbury, NY) in force calibration mode was used to determine

stiffness of the microfabricated pillars by measuring their spring constant. The substrate was cleaved and mounted on the microscope stage so that its cross section was exposed in a horizontal position. An AFM tip with a rectangular cantilever of known spring constant was used to record force curves on the rigid part of the cleaved substrate and on the free end of the pillar, which enabled the determination of the pillar's spring constant. The spring constant was determined by applying the equation $k_p = k_t \cos\theta\, Z_f / (Z_f - Z_r)$, where k_p is the spring constant of the pillar, k_t is the spring constant of AFM tip cantilever ($k_t = 0.283$ N/m, CLFC-NOBO calibration tip from ThermoMicroscopes, Sunnyvale, CA), θ is the inclination angle of the AFM tip cantilever ($\theta = 10°$ for Dimension 3000 NanoScope), and Z_r and Z_f are the vertical displacement of the AFM tip when the same force is applied on the rigid part and the flexible end of the microfabricated pillar, respectively (17,23). Four pillars were measured on a force sensor chip taken from the same wafer as the chips used in the cell experiments. The mean spring constant and standard deviation was calculated from these four measurements.

Cell culture

Passaged primary human vascular endothelial cells (EC) were obtained from the Wallenberg Laboratory for Vascular Research (Department of Surgery and Vascular Surgery, Sahlgrenska University Hospital, Gothenburg, Sweden). They were routinely cultured in T25 flasks (Greiner, Bio-One North America Inc., Monroe, NC; 1:2) in a standard tissue culture incubator at 37°C, 100% humidity, and 5% CO_2. Medium M199 (Gibco BRL, Gaithersburg, MD) was supplemented with 25 mM HEPES, 20% fetal calf serum (PAA Laboratories GmbH, Pasching, Austria), 2 mM L-glutamine, penicillin, streptomycin, 0.15 mg/ml ECGF, and 5000 IU/ml heparin (Sigma, St. Louis, MO). The EC cells used in this study were from the passage 5.

Passaged primary human fibroblasts (Wallenberg Laboratory for Vascular Research) were routinely cultured in T25 flasks (Greiner, 1:4) in a standard tissue culture incubator at 37°C, 100% humidity, and 5% CO_2. High-glucose Dulbecco's modified eagle medium (DMEM) (PAA Laboratories) was supplemented with 10% fetal calf serum (PAA Laboratories). For time-lapse microscopy, cells were detached with 1× trypsin-EDTA solution (Sigma, St. Louis, MO) and plated, as per routine passage. The fibroblasts used in this study were from the passage 7.

The EC were allowed to attach for an hour before observation, the fibroblasts were observed ~30 min after plating.

Digital microscopy of live cells

For live cell observation, microfabricated silicon substrates were placed in 35-mm tissue culture dishes (Nalge Nunc International, Rochester, NY) and sterilized by immersion in 70% ethanol, washed in Dulbecco's phosphate buffered saline (PBS) (PAA Laboratories) and equilibrated for a few minutes in complete medium before seeding of cells. Images were acquired every 3 and 5 min (for fibroblasts and EC, respectively) using a Zeiss ×40, NA 0.80 Achroplan immersion objective on a Zeiss Axioplan 2E imaging microscope equipped with differential interference contrast (DIC) optics, Zeiss Axiocam digital camera, and Zeiss Axiovision software (Carl Zeiss Light Microscopy GmbH, Göttingen, Germany). The use of reflected DIC was necessary due to the substrate's opacity. A thin film of sterile mineral oil (Sigma) was placed on top of the media to prevent evaporation. The culture was maintained at 37°C by an on-stage incubator (PDMI-2, Harvard Apparatus, Holliston, MA) and heating controller (TC-202A, Harvard Apparatus).

Image analysis

Image analysis was performed on stacks of uncompressed 8-bit grayscale TIFF images. Custom Matlab codes were used to process time-lapse sequences in Matlab 7.1 (The MathWorks, Natick, MA) with the following steps:

Generation of an "ideal lattice"

The ''ideal lattice'' represents the imaged array of undeflected pillars in the absence of cells. The image background was calculated using an opening operation and removed. The pillars were then identified in the background-subtracted image, using a thresholding operation. The center-to-center pitch between adjacent pillars in the x-direction was calculated by measuring the distance between pillars for all neighbors in a direction specified by the user. The pitch in the y-direction was calculated similarly, with a shift in angle of 90°. Using these pitches, a square ideal lattice was created. To correct for distortions in the real pillar lattice due to sample tilt or uneven illumination, pillars in the image were compared to the ideal lattice. Displacements in the x- and y-direction were separately mapped onto the z axis to visualize the displacements as a surface. A cubic surface was fitted to each of these mappings, and the pillar locations in the ideal lattice were shifted to obtain best agreement between the ideal lattice and the pillars in the first image in the sequence.

Corrections for substrate drift and rotation between images

Drift between subsequent images in a time-lapse sequence was corrected by tracking the median displacements of all pillars in the field of view (FOV). Rotation was corrected by minimizing the summed absolute displacement of all pillars due to rotation of the sample.

Measurement of pillar deflections and calculation of force vectors

Deflections were measured as the lateral displacement of the center of mass for each pillar. The force vectors were calculated assuming the pillars as standing cantilevers that behave as ideal springs, as described by Hooke's Law, $F = -kx$, with a spring constant k and lateral deflection x. The displacement of each pillar in each image of the sequence was calculated by comparing the center of mass of the pillar in the current image with the center of mass of the same pillar in the ideal lattice. The force vectors were then superimposed on each image of the sequence. Contrast and brightness corrections were used after analysis to enhance cell detail for Figs. 3 and 4.

Processing DIC images to reveal flat cells

The enhancement process was based on rapid shifts in intensity that occur inside the cell body, and the ruffling of the cell perimeter. These shifts were visibly larger than the image noise, but most easily seen in a video sequence of cells. To visualize this in a single image, a batch of 11 images centered on the current frame was extracted from the sequence. The batch images were corrected for differences in background illumination, and the enhanced image was calculated by summing up the absolute differences between the current image and the neighboring frames in the image batch. The results were saved as separate 8-bit TIFF image files. These enhanced images were not used for force measurements.

Orientation of force vectors

Force vectors were further classified with respect to the direction of cell spreading. The center of a cell was manually marked; the vectors were designated either positive or negative, by the sign of the comparison of the distance between the cell center and the shifted pillar location, and the distance between the cell center and the original pillar location. A positive vector is thus oriented away from the center of the cell, and similarly, a negative vector is oriented toward the cell center.

Determination of contact guidance and cell speed

EC alignment was derived from the 5-min interval time-lapse images. Cells were manually outlined in enhanced images. Elongation was calculated as the ratio of the distance between the foci and the major axis length of an

ellipse with the same second-moments as the outlined cell. Elongation values fall between 0 (*circle*) and 1 (*line*). Alignment angle was then defined as the absolute value of the angle between the ridge orientation and the major axis of that ellipse. Movement angle was calculated as the absolute value of the angle between the ridge orientation and the displacement vector of the center of mass for each cell for the 5-min interval. Cell speed was calculated as the length of that displacement vector. A cell was classified as contact guided if the following criteria were met: cell alignment angles of $<10°$ compared to the ridge direction and, where appropriate, movement angles of $<10°$ for a minimum duration of 15 min.

RESULTS

Silicon wafers were micropatterned by photolithography and deep reactive ion etching to form rows of 2 μm diameter and 51 μm high vertical pillars, with $\sim$3 μm^2 attachment pads at the top of the pillars (Fig. 1). Rows of pillars were located in trenches between solid ridges of 6 or 8 μm in width for EC and fibroblast cell samples, respectively. Correspondingly, the pillar array had pitch patterns of 4×12 or 4×14 μm^2. The spring constant of the pillars was 116 ± 10 nN/μm, as determined from measured AFM force curves (17). The silicon dioxide surface of the wafer was visualized along with the cells by reflected DIC microscopy, and measurements of pillar displacement were made from DIC images based on the ideal lattice—an estimation of the true resting position of pillars, because cells were present in all images of the recorded time-lapse sequences and could influence the initial positions of some of the pillars. To understand the direction of the force vectors in Figs. 3 and 4 (represented as *straight white lines*) one must note that the origin of the vector is at the position of the ideal lattice.

Endothelial cell motility and contact guidance

We observed various behaviors of EC on ridged force sensor chips during time-lapse sequences. EC were observed with examples of stationary or migratory behavior, as well as rounded or elongated morphology, and contact guidance. However, the majority of EC observed exhibited clear alignment to the ridge pattern and/or contact guidance. Fig. 2, *A–C*, contains images taken from a time-lapse sequence of EC positioned at a corner of the force sensing area of a chip. At the start of image acquisition, i.e., 1 h postseeding (Fig. 2 *A*), a flattened, discoid cell (labeled EC 1) with a ruffled membrane became elongated and moved from the flat to the force sensing area of the substrate in a direction approximately perpendicular to the ridges (Fig. 2, *B* and *C*). The advancing front of EC 1 remained spread as it moved across the rows of pillars with a mean speed of 0.53 μm/min and a maximum speed of 0.97 μm/min, the latter measured as the cell body was retracted. Cell elongation, alignment, and angle of cell movement data during the first 90 min of the image sequence are indicated in Fig. 2, *D–F*. During the first 20 min of image acquisition, EC 1 goes from being round, with an elongation of 0.47, to having an elongation of 0.8. The elongated EC 1 moved onto the patterned area at an average movement angle of 63° with respect to the orientation of the ridges. As EC 1 moved further onto the patterned area, the alignment angle of the cell decreased from $\sim$80° (observed from 20–60 min) to $\sim$0° (by 90 min), indicating that the cell body was beginning to align with the ridges.

In contrast, a second cell (labeled EC 2) in Fig. 2, *A–C*, moved from the flat surface to the force-sensing area of the substrate in a direction parallel to the ridge orientation. EC 2 also became highly elongated (elongation 0.98, Fig. 2 *D*) as it moved onto the pattern but did not remain spread. Instead, EC 2 aligned to the pattern (mean alignment angle 1.7°, Fig. 2 *E*), and moved along the ridge (mean movement angle 0.4°) from 30 min onward (Fig. 2 *F*), with mean speed of 0.96 μm/min and maximum speed of 2.11 μm/min. As both alignment and movement angle were within 10°, EC 2 clearly fulfilled the criteria for contact guidance. A third elongated and aligned cell in Fig. 2, *A–C*, (EC 3, at *center top of image*) was present on the pattern at start of acquisition, but remained stationary during the course of the sequence. Cell traction force analysis was performed on the EC time-lapse sequence in Fig. 2. A selected area of this sequence is shown in Fig. 3 (*boxed area* in Fig. 2 *A*). DIC images obtained at 0, 30, 45, 60, and 75 min into the sequence are shown in Fig. 3, *A–E*. They contain superimposed white lines that indicate the measured force vectors exerted on the pillars. The contrast in these images has been increased post-force-analysis to enhance the cell detail. The images in Fig. 3, *F–J*, have been further enhanced, as described in the Materials and Methods section ''Processing DIC images to reveal flat cells'', to aid in identification of the total cell area. As a result of this image processing procedure, the pillars appear larger in diameter than their actual size.

We observed dynamic motion of pillars under migrating and stationary EC, and forces up to 57 nN were recorded (Fig. 6). Multiple pillars were positioned and deflected under each cell, and their deflections were dynamic and independent. Many force vectors were detected at the leading and trailing edges of the cells, this being especially the case for

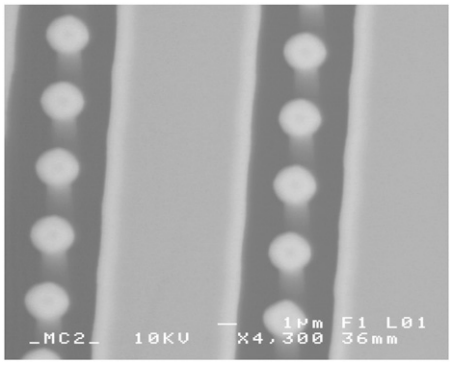

FIGURE 1 Scanning electron microscope image of the force sensor showing the arrangement of ridge and pillar structures. Pillars exist in single rows between ridges, and the surfaces of both are at the same height (image taken at a slight angle). Scale bar indicates 1 μm.

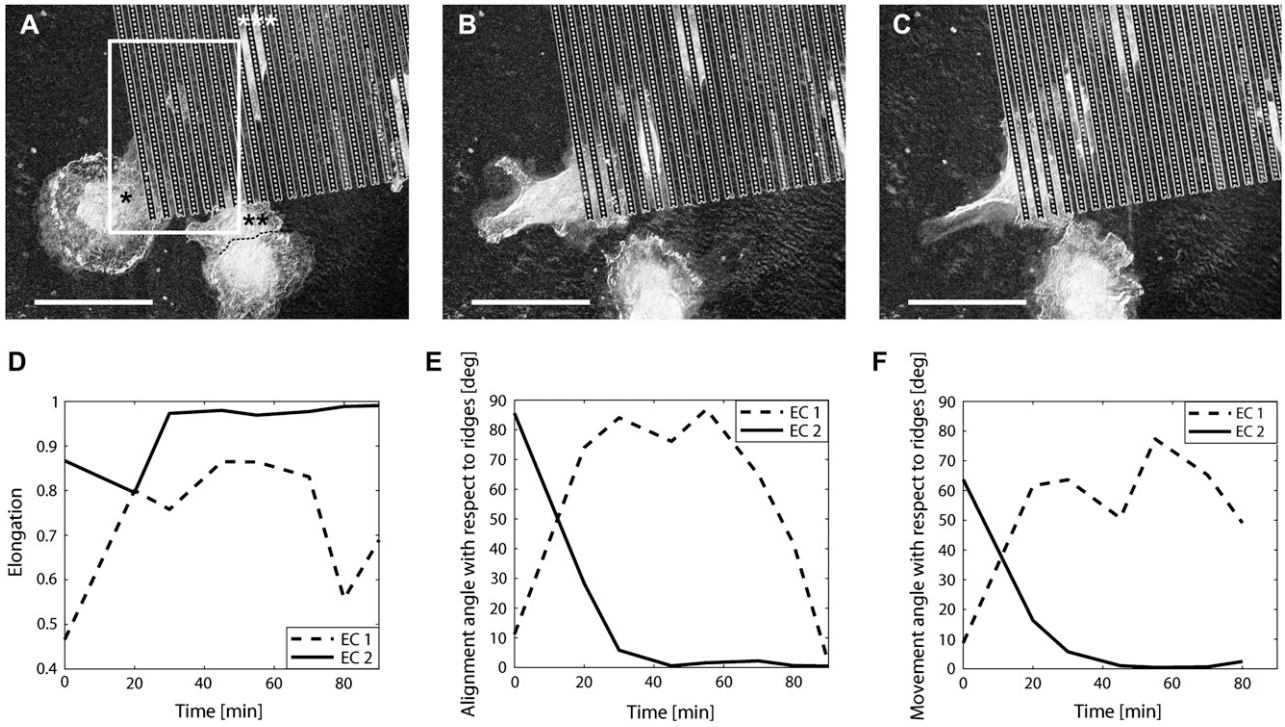

FIGURE 2 (*A–C*) Enhanced images of EC on a ridged cell force sensor at 0, 60, and 90 min into image acquisition, respectively. Three specific cells are identified in this image: EC 1 (marked with *), EC 2 (marked with **), and EC 3 (marked with ***). Note that in panel *A*, EC 2 is in contact with another cell so the cells have been separated by a dotted line. Scale bar indicates 100 μm. (*D* and *F*) Determination of contact guidance for EC. Elongation, alignment, and movement values are plotted for EC 1 and EC 2 to show difference between a migrating cell, and a cell that is contact guided, respectively. (*D*) Cell elongation is plotted versus time of image acquisition. Elongation 0 represents a circle, 1 represents a line. EC 2 is clearly very elongated after 30 min into the sequence. (*E*) Alignment angle with respect to the ridges is plotted over time. An angle of 0° describes the cell as being parallel to the ridge orientation. An angle of 90° describes the cell as perpendicular to the ridge orientation. EC 2 is clearly aligned with the pattern from 30 min into the sequence, onward. (*F*) Movement angle with respect to the ridges is plotted over time of image acquisition. An angle of 0° describes movement that is parallel to the ridge orientation. An angle of 90° describes movement that is perpendicular to the ridges. EC 2 is clearly moving along the ridges from 30 min into the sequence and onward.

the contact-guided cell EC 2. The forces generated by the contact-guided EC 2 showed a lower maximum (31 nN) than EC 1 (57 nN), though the force distributions were otherwise similar (data not shown). Naturally, fewer forces were measured under EC 2 compared with EC 1, due to the fivefold difference in area (mean area 3371 and 674 μm^2, respectively). One of the pillars (Fig. 3, third pillar row from left, 13 pillars from patterned edge) shows a spurious deflection due to a mismatch with the ideal lattice, which is altered once the cell is overlying it. (This type of error could be selectively excluded from the analysis if desired.)

Spreading fibroblast cell

The fibroblasts were observed starting at 30 min after seeding in an attempt to acquire more data during the attachment and spreading phases. The fibroblasts observed in the time-lapse sequence were in general round and not elongated or aligned to the orientation of the ridges. The mean elongation of 13 cells, completely contained within the FOV at 3 h 12 min into the sequence, was 0.66 (SD 0.17) and mean alignment angle was 39° (SD 29°), which does not indicate an alignment trend at this time point. In addition, the fibroblasts showed limited migratory behavior and none of the cells observed in the FOV throughout the entire sequence ($n = 19$) exhibited contact guidance. An example of a spreading fibroblast from this sequence is found in the center of the field of view in Fig. 4. This cell is round in contrast to the neighboring cell that is more flattened and spread. In the observed population, the ratio of round to spread cells at the start of image acquisition was 2:1. Images obtained at 0, 30, 60, 120, and 240 min into the sequence are shown. The DIC images in Fig. 4, *A–E*, show superimposed white lines that indicate the measured force vectors exerted on the pillars. The contrast in these images is increased to observe the cell detail. The images in Fig. 4, *F–J*, have been processed to further enhance the contrast and aid in identification of the total cell area in the image, as described in the Materials and Methods section ''Processing DIC images to reveal flat cells''. As a result of this image processing, the pillars appear larger in diameter than their actual size.

During the entire 360-min sequence, of which a selected area is depicted in Fig. 4, we observed that the majority of force vectors generated by the cell at the center of the field of view were oriented in the direction of cell spreading (i.e., radially outwards) during the beginning of the sequence, but

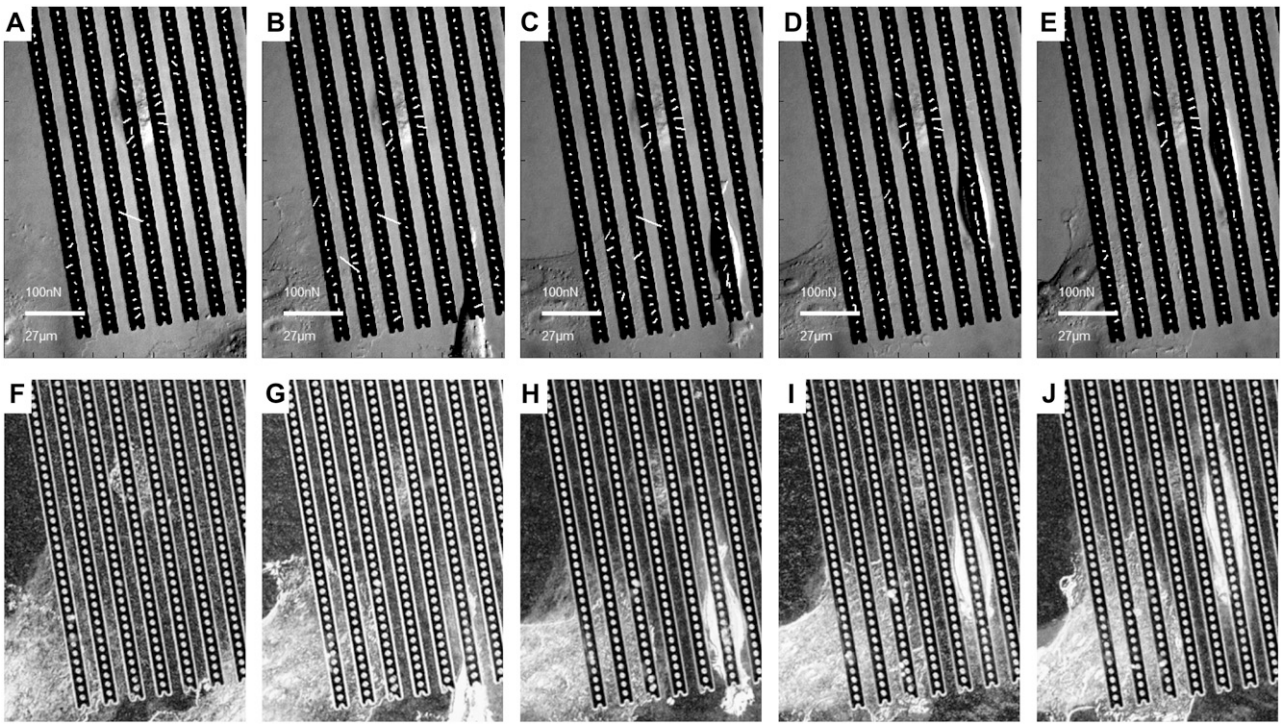

FIGURE 3 (*A–E*) DIC images taken from the white boxed area shown in Fig. 2 of EC on a ridged cell force sensor at 0, 30, 45, 60, and 75 min into image acquisition, respectively. The superimposed white lines indicate force vectors exerted on the pillars. EC 1 (*bottom left*) migrated perpendicular to the patterned pillars, EC 2 (*bottom right*) approached parallel to the patterned area, and EC 3 remained stationary throughout the sequence (*center*). (*F–J*) Corresponding DIC images of panels *A–E* enhanced to show cells in better detail. Scale bars indicate 27 μm for length scales, and 100 nN for force vectors.

then switched to be oriented opposite to the direction of spreading (i.e., radially inwards) with time. Pillars with force vectors oriented toward the cell center (i.e., inwards) have been circled in Fig. 4, *A–E*. The number of inwardly directed force vectors under this cell increased with time. Note that pillars located under the portion of the cell, which is in contact with the other cell in the field of view (at *upper right*), have been neglected from this analysis. A cartoon to describe this observation is shown in Fig. 5 *A*. It illustrates a cell spreading from both a top and side view. The dotted line represents the cell perimeter at early time points, whereas the solid line represents the cell perimeter at later time points

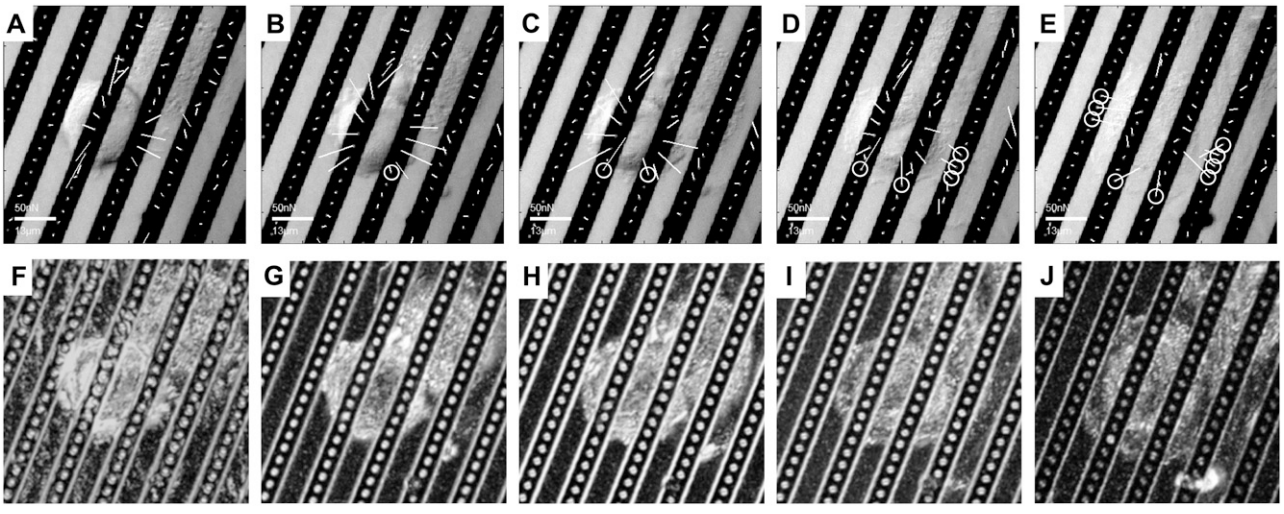

FIGURE 4 (*A–E*) DIC images of fibroblast cells on a ridged cell force sensor at 0, 30, 60, 120, and 240 min into image acquisition, respectively. Note that there are two cells in the image: one spreading cell in the center and one already spread cell in upper right. White lines indicate force vectors. White circles show force vectors under the cell that are oriented opposite to the direction of spreading. (*F–J*) Corresponding DIC images of panels *A–E* enhanced to show cells in more detail. Scale bars indicate 13 μm for length scales, and 50 nN for force vectors.

in the spreading process. Dark gray arrows show the forces oriented in the direction of cell spreading. Light gray arrows indicate forces oriented away from the direction of cell spreading.

To better describe this behavior, we tracked the magnitude and direction of each pillar in the field of view acquired at each time point of the sequence shown in Fig. 4. Fig. 5 *B* shows the same field of view and time-lapse sequence from Fig. 4, however, now the pillars have been numbered and the distribution of forces observed within this field of view with time have been plotted in Fig. 5, *C* and *D*. In Fig. 5 *C*, force values for pillars under the cell at center and those surrounding, but never in contact with the flattened cell, were plotted as a function of time. Included in the plot are pillars numbered 164–168, 141–150, 116–124, 92–99, and 67–70. A positive force represents force vectors oriented away from the center of mass of the cell, whereas a negative force represents force vectors oriented toward the center of mass of the cell. Because forces for all pillars (i.e., both those under and those not under cells) are plotted, there is a noise band in our measurements between ±5 nN, which is densely packed with data points. The most remarkable result is the transition from largely positive to largely negative forces at ~125 min into the sequence.

Fig. 5 *D* shows a simplified version of the same plot, indicating the forces measured on two sets of six pillars located in adjacent rows. The first set (pillars numbered 114–119) represents those pillars positioned under the cell (*dark gray*), and the second set (pillars numbered 140–145) those not under the cell (*light gray*), at start of the time-lapse acquisition. The solid black line in Fig. 5 *D* represents a single pillar, number 162, which was never in contact with either of the cells. Forces measured in the first ~150 min of the sequence were exclusively those pillars located under the cell, and were oriented with the direction of cell spreading; whereas those forces measured in the latter half of the sequence are for pillars that the cell had spread onto and were oriented against the direction of spreading. We have observed outward spreading forces in other spreading cells in the full FOV, however, the time for transition and clarity of this transition varied between cells.

In addition to the observation of a transition in force orientation, the plot in Fig. 5 *D* also demonstrates the elasticity of the pillars as many resumed their original resting positions when the spreading cell had advanced beyond them and begun deflecting pillars in the adjacent row. Likewise, the pillars in the adjacent row show no deflections until the cell is in contact with them, though a noise band of the range of ±5 nN is apparent in the absence of any force thresholding.

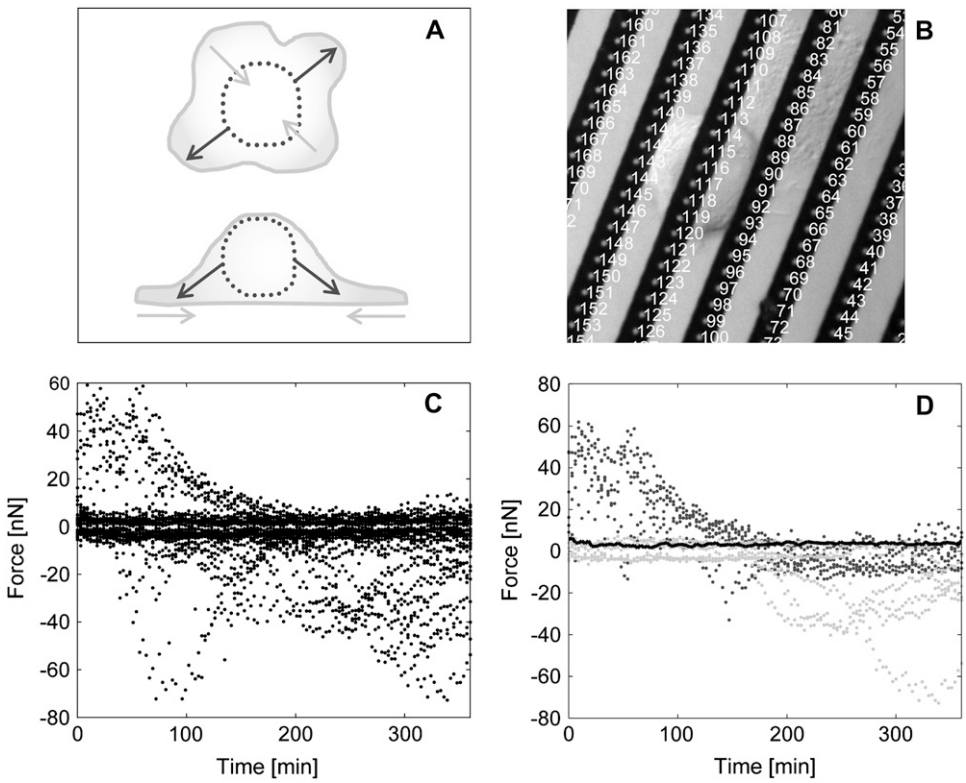

FIGURE 5 (*A*) A cartoon of a spreading cell viewed from the top and side. The dotted line represents the cell perimeter at early time points, whereas the solid line represents later time points in attachment and spreading. Dark gray and light gray arrows indicate forces oriented in, and opposite to, the direction of spreading, respectively. (*B*) The same FOV shown in Fig. 4 with numbered pillars. (*C* and *D*) Plots of forces over time for individual pillars located in this FOV, indicating a transition in force orientation with regard to spreading direction of centrally located cell. Positive and negative forces are oriented away from and toward the center of the cell, respectively. (*C*) Includes all pillars in the frame except those in contact with the already spread cell at upper right and, thus, has a dense noise band at ±5 nN. The strong inward forces (below −40 nN) during the initial 150 min of observation are indicated only by a single pillar number 120. (*D*) Plot of forces over time for a row of six pillars under the spreading cell at start of image acquisition (*dark gray*) and six pillars in the adjacent row not under the cell until later time points (*light gray*). A pillar never in contact with any cell is shown with a black line. The transition from mainly positive to negative forces is clear.

Summary of traction forces

Fig. 6 contains a histogram of all forces detected in the fibroblast sequence (*solid line*) and EC sequence (*dashed line*). Data are obtained from all pillars in the full time-lapse sequences shown in Fig. 2 (EC) and Fig. 4 (fibroblasts). Note that Figs. 4 and 5 contain a selected portion of the full field of view of the fibroblast time-lapse sequence data included in Fig. 6. The data is represented as the fraction of total force measurements falling into each bin, with a bin size of 4 nN. The EC data contains 33,869 force measurements obtained from an FOV containing an average number of five cells on the force sensing area throughout the time course of the sequence. This data were collected over a sequence of 100 frames taken at 5-min intervals. The fibroblast data contains 113,027 force measurements obtained from an FOV containing an average number of 19 cells on the force sensing area throughout the time course of the sequence. This data was collected over a sequence of 121 frames taken at 3-min intervals. A logarithmic scale on the *y* axis was used to place emphasis on the higher forces measured under the cells with respect to the noise, which would otherwise dominate the plot because there are more pillars around than under cells.

To estimate nonspecific forces due to image noise detected by the analysis routines, a portion of the force sensor chip void of cells was also processed. The distribution of forces detected in a portion of the FOV from the fibroblast sequence containing no cells is shown in Fig. 6 (*dotted line*). A total of 1818 measurements were included in this data set. The mean force was 3.29 nN (SD 2.23 nN); 95% of the forces were lower than 7.2 nN (99% $<$ 8.7 nN, 99.9% $<$ 11.2 nN). Thus we claim to have a sensor sensitivity of 7.2 nN. Forces of larger magnitude than the measured nonspecific forces were observed for both cell types. The fibroblasts exerted a greater range of forces, up to 138 nN, than did the EC, up to 57 nN.

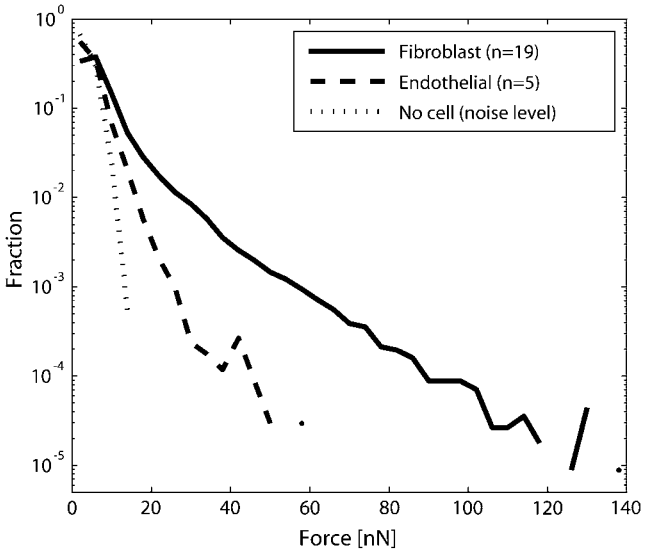

FIGURE 6 Histogram of forces measured in fibroblasts and EC, compared with forces measured in an empty FOV. The histogram has a logarithmic *y* axis and is normalized to the number of force measurements for each cell type; *n* denotes number of cells, wholly or partially in the FOV.

DISCUSSION

Despite the preliminary nature of the results presented in this study, we believe the potential of micromachined silicon in the production of force-sensor substrates for the measurement of cell forces in the nanonewton range is clearly demonstrated. The incorporation of topographical features into the force-sensor substrates, in this case micron-sized ridges, has allowed the possibility to induce changes in morphology and migratory behavior of cells while simultaneously detecting traction forces. The force sensor chips evaluated in this study were intended to induce contact guidance of cells. Although it is also possible to define the chemical properties of the substrates, in this report we showed cell attachment with adsorbed serum proteins alone.

For EC, a microgrooved pattern can (24) and, on our ridged sensor chips, did induce changes in cell shape and motility associated with contact guidance. One cell (EC 1) approached perpendicular to the pattern and remained spread as it moved across the rows of pillars, whereas the second cell (EC 2) approached parallel to the patterned ridges, became highly polarized, and remained aligned to the pattern as it moved along the ridge. The measured alignment and movement angles of 1.7° and 0.4°, respectively, for the latter cell were clearly parallel to the pattern and well within the limits set for contact guidance. The elongation value of 0.98 for this cell indicated how extreme the morphology change was once the cell contacted the pattern. This provided further validation of the alignment angle because a cell that is almost round has no alignment value of interest. Differences in the forces measured for the contact-guided and non-contact-guided EC need to be confirmed by additional measurements to allow proper statistical analysis. It is possible to reason that there should be differences in cell traction forces between contact-guided and non-contact-guided cells. Using the example of EC 1 and EC 2 observed in this study, there are differences in cell-substrate contact area (fivefold) as well as duration of contact. The first, more spread cell (EC 1) was, during the entire period of observation, overlying more pillars than the elongated contact-guided cell (EC 2). There could additionally be a contribution from differing migration speeds, because a slow moving cell has more opportunity to develop mature focal adhesions. As an example, in a comparison of force measurements performed on a slow cell type, like fibroblasts (6), with those on a fast cell type, keratocytes (25), a 60-fold increase in mean migratory speed equated to a 10-fold decrease in stress on the surface.

Our observations on the initial stages of fibroblast spreading show a noticeable and unexpected feature. Initially, pillars located under a round cell appeared deflected outward and oriented with the direction of spreading. Later (at ~150

min into the image sequence for the cell shown in Figs. 4 and 5 and ~180 min after seeding) as the cell became flattened, a transition in force orientation occurred and the pillars were then observed to be deflected inward, against the direction of spreading. The fibroblasts we observed attached directly on the pattern. During the course of the sequence, they spread and contacted other cells, but did not undergo any major morphological changes or migration. Fibroblasts have previously been shown to exhibit contact guidance when grown on ridged substrates (26,27). For those fibroblasts imaged on our sensor that were entirely within the FOV, mean alignment angle was 39° (SD 29°) and mean elongation was 0.66 (SD 0.17), which does not indicate any alignment trend. Analysis on the distribution of force vector angles was performed (data not shown) and it was concluded that the direction of cell traction forces associated with spreading did not appear to be influenced by ridge orientation. At the cell seeding density used in this study, influence from cell-cell contacts cannot be excluded from the interpretation of the results and can play a role in the behavior of the fibroblast cell analyzed in Figs. 4 and 5. However, all fibroblasts found to have a rounded morphology similar to the cell shown in Figs. 4 and 5 exhibited initially outward spreading forces. The time for a force direction transition and clarity of this transition varied between these cells, most likely due to the cells being in different stages of the attachment/spreading process. Again, the influence of cell-cell contacts cannot be excluded. Our current experimental setup does not allow immediate imaging of cells directly at time of seeding. However, an improvement to this setup would include the use of microinjection pipette to place an individual cell under the field-of-view after the start of the time-lapse sequence. In this way we would both avoid cell-cell contacts and observe the entire attachment and spreading events. Similarly, the use of an isotropic cell force sensor design, such as a chip without a ridge pattern or overriding orientation, would be more suitable for future studies of changes in force direction for attaching and spreading cells.

In previous studies of initial EC attachment and spreading, traction forces were evident already in early spreading and typically pointed inward throughout the entire process of spreading (28). Cells were capable of exerting significant forces before either notable focal adhesion or stress fiber formation (28) and these early forces were attributed to other mechanisms of force transduction. Maximum stress fiber content in EC was observed to peak at ~150 min after cell seeding. The occurrence of new binding events of ligand-receptor interactions was assumed to be completed by that time. Our observations with early spreading fibroblasts show a change in force direction, and which might be attributed to a similar maturation in the focal contact-cytoskeletal machinery allowing contractile forces to be generated. The use of live fluorescent labels of the cytoskeletal and focal contact machinery would allow us to correlate these events with observed forces. We did not observe any transition in force orientation for EC because the cells were already spread at start of image acquisition. This discrepancy between directions of forces for attaching and spreading EC reported in the study by Reinhart-King et al. (28) and our early spreading fibroblasts could be attributed to the different cell types having different behavior; however, the differences in force-sensing substrates cannot be excluded. The magnitudes of cell traction forces measured (28,29) were somewhat lower than those we report, however, it is not straightforward to make a comparison between discrete forces, as we measure, and a force average over an entire cell.

Passaged human EC and fibroblast cells attached to and spread on the silicon dioxide-covered silicon wafer substrates and deflected the microfabricated pillars. ECs were observed to align with the ridge and groove pattern as well as exhibit contact guidance in migration. However, fibroblast cells were not observed to elongate, align, or exhibit contact guidance under the conditions tested. The different cell types thus showed markedly different morphology and behavior on the ridged force sensing substrate. Although the ridge width used in the culture of EC was 2 μm narrower than used for testing fibroblasts, the pillar dimensions were the same. It is possible that the larger ridge width prevented fibroblasts from aligning and experiencing contact guidance, as fibroblasts have previously been reported to be sensitive to ridge width, height, and pitch on microgrooved substrates (18,30,31) The five EC and 19 fibroblasts included in the presented data produced an almost continuous range of forces up to 57 and 138 nN, respectively. The magnitude of force observed for fibroblasts was higher than in several previously reported results (6,12,13) but, similarly to the EC result, the difference in methods makes the comparison unreliable. Given that the force data are a range and do not have a normal distribution, a mean value and standard deviation is not as representative as showing the distribution in its entirety, and rather, may be deceptive in the information it appears to give. Therefore we do not include this type of analysis, opting instead to show the full force distributions.

The dimensions and sensitivity of the patterned, pillared, force sensing substrates were such that multiple pillars could be deflected independently under each cell. Tracking a group of pillars over time showed that pillar deflections were elastic, returning to their resting positions when not actively deflected by the cell. In this study, forces were measured in a range up to 138 nN. Nonspecific force vectors, i.e., vectors measured in the absence of cells, were presented in Fig. 6. The sensitivity of 7.2 nN obtained from this data set, combined with the spring constant of the pillars, and the scaling factor of the image results in the spurious noise being <0.25 pixels. We believe this noise level is quite acceptable and is indicative of the quality of our images and analysis routines. Therefore, to increase the sensitivity of the sensor, pillars with lower spring constants could be used. This would be theoretically possible because the highest measured force of 138 nN is clearly lower than the total force needed for a

collision of two neighboring pillars (232 nN). The individual force measurements are affected by a nonspecific error of mean value 3.29 nN but, because the errors are evenly distributed in all directions, the effective measurement error would be lower. Factors contributing to the measurement error could include imperfect correction of shift, debris, image distortion, and artificial vectors on pillars imperfectly aligned with the ideal lattice. Forces exerted on standing silicone (PDMS) pillars have previously been reported to be up to 60 nN, with individual pillars reaching even 90 nN for smooth muscle cells, and this substrate was shown to have a standard deviation of spurious forces of 12 nN (14). The authors therefore claim to resolve forces >12 nN. Another group using pillared silicone substrates reported a range of forces from 10 to 30 nN for human fibroblast cells, claiming a resolution of 4 nN with an error of at least 20% (12). Thus our rigid silicon pillar sensor performs as well as, if not better than, other pillared cell traction force sensors described in the literature.

The advantages of using patterned silicon substrates as cell force sensors include excellent optical contrast, a large attachment area at the top of each pillar, batch processing, and robust structure. The pillars are mechanically isolated so forces exerted on one pillar will not influence the deflection of others unless they touch due to extremely large deflections. Such large deflections have not been observed and, due to the stiffness of the pillars, are not expected. The disadvantages of the patterned silicon substrates are that calibration is labor and cost intensive and that their fabrication requires both clean-room facilities and specialized equipment. In addition to the choice of material, the use of DIC microscopy enabled acquisition of high-contrast images of cell-substrate interactions over time on the nontransparent sensors. The images had a very low noise level, which is essential for both cell force measurement and image enhancement. By using time-lapse microscopy, the sampling rate can be tuned to capture the process(es) of interest and there is no artifactual force detection, such as shrinkage from cell fixation procedures. The image enhancement routine developed in this work, based on intensity shifts in pixels over time, allows for better visualization of cell perimeters and detection of boundaries between neighboring cells compared with standard brightness and contrast enhancements. This is due to the fact that the most rapid intensity shifts in the DIC image are in the ruffling membrane, where the cytoskeleton is actively remodeled. Standard brightness and contrast enhancements have limited effect in cells where the membrane is spread thin. However, with contrast being generated by differences in refractive index, it could still be advantageous to image cell and substrate in separate optical channels. In the absence of postprocessing, flattened, spreading cells may be difficult to distinguish from the background, whereas imaging thicker cells would move the focus away from the surface. The use of a fluorescence-labeled cell line, focal adhesion protein, or labeled pillar tops would allow imaging of cells and pillars separately, and would therefore provide a more detailed perspective of the relationship between cell (shape) and traction forces. Furthermore, this would also elucidate whether the cell is in fact attached to the tops, or penetrating the etched trenches to partially engulf the pillars—a factor of particular interest for pillared sensors with lower aspect ratios, such as those in PDMS, where cells might have access to the basal surface.

In summary, the technique of using micron-sized pillars as force sensors in cell traction studies and the use of micropatterned ridges to influence cell elongation, alignment, migration, and contact guidance have both been shown previously. In this pilot study we present the possibility of combining these two established techniques in a rigid material and, as an example, measuring cell forces in two physiologically relevant cell models. The observations presented here indicate proof-of-function of the ridged cell force sensor to induce contact guidance, and that the pillared cell force sensor constructed in rigid silicon has the necessary sensitivity to detect differences in traction force vectors between different cell phenotypes and morphologies. With the possibility to incorporate force sensing with topographical and chemical cues, we predict that these substrates may be designed to influence movement and mechanical substrate interaction for various adherent cell types.

The authors thank Prof. Bo Risberg and Dr. Sepideh Hagvall (Wallenberg Laboratory for Vascular Research, Department of Surgery and Vascular Surgery, Sahlgrenska University Hospital, Gothenburg, Sweden) for valuable discussions and the contribution of both EC and fibroblast cultures.

Financial support was received from the ''Biocompatible Materials'' program of the Swedish Foundation for Strategic Research (SSF), the Swedish Council for Research (VR), and the Chalmers Bioscience Program (CBP).

REFERENCES

1. Huang, S., and D. E. Ingber. 1999. The structural and mechanical complexity of cell-growth control. *Nat. Cell Biol.* 1:E131–E138.
2. Wong, J. Y., J. B. Leach, and X. Q. Brown. 2004. Balance of chemistry, topography, and mechanics at the cell-biomaterial interface: issues and challenges for assessing the role of substrate mechanics on cell response. *Surf. Sci.* 570:119–133.
3. Harris, A. K., P. Wild, and D. Stopak. 1980. Silicone rubber substrata: a new wrinkle in the study of cell locomotion. *Science.* 208:177–179.
4. Lee, J., M. Leonard, T. Oliver, A. Ishihara, and K. Jacobson. 1994. Traction forces generated by locomoting keratocytes. *J. Cell Biol.* 127: 1957–1964.
5. Pelham, R. J. Jr., and Y. Wang. 1997. Cell locomotion and focal adhesions are regulated by substrate flexibility. *Proc. Natl. Acad. Sci. USA.* 94:13661–13665.
6. Dembo, M., and Y. L. Wang. 1999. Stresses at the cell-to-substrate interface during locomotion of fibroblasts. *Biophys. J.* 76:2307–2316.
7. Pelham, R. J., Jr., and Y. Wang. 1999. High resolution detection of mechanical forces exerted by locomoting fibroblasts on the substrate. *Mol. Biol. Cell.* 10:935–945.
8. Balgude, A. P., X. Yu, A. Szymanski, and R. V. Bellamkonda. 2001. Agarose gel stiffness determines rate of DRG neurite extension in 3D cultures. *Biomaterials.* 22:1077–1084.

9. Dubey, N., P. C. Letourneau, and R. T. Tranquillo. 2001. Neuronal contact guidance in magnetically aligned fibrin gels: effect of variation in gel mechano-structural properties. *Biomaterials.* 22:1065–1075.

10. Freyman, T. M., I. V. Yannas, R. Yokoo, and L. J. Gibson. 2002. Fibroblast contractile force is independent of the stiffness which resists the contraction. *Exp. Cell Res.* 272:153–162.

11. Chicurel, M. E., C. S. Chen, and D. E. Ingber. 1998. Cellular control lies in the balance of forces. *Curr. Opin. Cell Biol.* 10:232–239.

12. Schwarz, U. S., N. Q. Balaban, D. Riveline, L. Addadi, A. Bershadsky, S. A. Safran, and B. Geiger. 2003. Measurement of cellular forces at focal adhesions using elastic micro-patterned substrates. *Mater. Sci. Eng. C-Biomimetic Supramol. Syst.* 23:387–394.

13. Galbraith, C. G., and M. P. Sheetz. 1997. A micromachined device provides a new bend on fibroblast traction forces. *Proc. Natl. Acad. Sci. USA.* 94:9114–9118.

14. Tan, J. L., J. Tien, D. M. Pirone, D. S. Gray, K. Bhadriraju, and C. S. Chen. 2003. Cells lying on a bed of microneedles: an approach to isolate mechanical force. *Proc. Natl. Acad. Sci. USA.* 100:1484–1489.

15. Tanaka, Y., K. Morishima, T. Shimizu, A. Kikuchi, M. Yamato, T. Okano, and T. Kitamori. 2006. Demonstration of a PDMS-based bio-microactuator using cultured cardiomyocytes to drive polymer micro-pillars. *Lab Chip.* 6:230–235.

16. Petronis, S., C. Gretzer, B. Kasemo, and J. Gold. 2003. Model porous surfaces for systematic studies of material-cell interactions. *J. Biomed. Mater. Res. A.* 66A:707–721.

17. Petronis, S., J. Gold, and B. Kasemo. 2003. Microfabricated force-sensitive elastic substrates for investigation of mechanical cell-substrate interactions. *J Micromech Microeng.* 13:900–913.

18. Dalby, M. J., M. O. Riehle, S. J. Yarwood, C. D. Wilkinson, and A. S. Curtis. 2003. Nucleus alignment and cell signaling in fibroblasts: response to a micro-grooved topography. *Exp. Cell Res.* 284:274–282.

19. Weiss, P., and B. Garber. 1952. Shape and movement of mesenchyme cells as functions of the physical structure of the medium: contributions to a quantitative morphology. *Proc. Natl. Acad. Sci. USA.* 38: 264–280.

20. Clark, P., P. Connolly, A. S. Curtis, J. A. Dow, and C. D. Wilkinson. 1990. Topographical control of cell behaviour. II. Multiple grooved substrata. *Development.* 108:635–644.

21. Charest, J. L., M. T. Eliason, A. J. Garcia, and W. P. King. 2006. Combined microscale mechanical topography and chemical patterns on polymer cell culture substrates. *Biomaterials.* 27:2487–2494.

22. Britland, S., H. Morgan, B. Wojiak-Stodart, M. Riehle, A. Curtis, and C. Wilkinson. 1996. Synergistic and hierarchical adhesive and topographic guidance of BHK cells. *Exp. Cell Res.* 228:313–325.

23. Tortonese, M., and M. Kirk. 1997. Characterisation of application specific probes for SPMs. *SPIE.* 3009:53–60.

24. Dike, L. E., C. S. Chen, M. Mrksich, J. Tien, G. M. Whitesides, and D. E. Ingber. 1999. Geometric control of switching between growth, apoptosis, and differentiation during angiogenesis using micropatterned substrates. *In Vitro Cell. Dev. Biol. Anim.* 35:441–448.

25. Doyle, A., W. Marganski, and J. Lee. 2004. Calcium transients induce spatially coordinated increases in traction force during the movement of fish keratocytes. *J. Cell Sci.* 117:2203–2214.

26. Brunette, D. M. 1986. Fibroblasts on micromachined substrata orient hierarchically to grooves of different dimensions. *Exp. Cell Res.* 164:11–26.

27. Walboomers, X. F., H. J. Croes, L. A. Ginsel, and J. A. Jansen. 1999. Contact guidance of rat fibroblasts on various implant materials. *J. Biomed. Mater. Res.* 47:204–212.

28. Reinhart-King, C. A., M. Dembo, and D. A. Hammer. 2005. The dynamics and mechanics of endothelial cell spreading. *Biophys. J.* 89:676–689.

29. Reinhart-King, C. A., M. Dembo, and D. A. Hammer. 2003. Endothelial cell traction forces on RGD-derivatized polyacrylamide substrata. *Langmuir.* 19:1573–1579.

30. Walboomers, X. F., W. Monaghan, A. S. Curtis, and J. A. Jansen. 1999. Attachment of fibroblasts on smooth and microgrooved polystyrene. *J. Biomed. Mater. Res.* 46:212–220.

31. Loesberg, W. A., X. F. Walboomers, J. J. van Loon, and J. A. Jansen. 2006. The effect of combined hypergravity and micro-grooved surface topography on the behaviour of fibroblasts. *Cell Motil. Cytoskeleton.* 63:384–394.